Limnol. Oceanogr., 57(3), 2012, 772–786

doi:10.4319/lo.2012.57.3.0772

The structure of basin-scale internal waves in a stratified lake in response to lake bathymetry and wind spatial and temporal distribution: Lake Iseo, Italy

Giulia Valerio,[a,*] Marco Pilotti,[a] Clelia Luisa Marti,[b] and Jörg Imberger [b]

[a] DICATAM, Facoltà di Ingegneria, Università degli Studi di Brescia, Brescia, Italy
[b] Centre for Water Research, The University of Western Australia, Crawley, Western Australia, Australia

Abstract

Field data, theoretical analyses, and numerical simulations were used to investigate the effects of lake basin bathymetry and spatial and temporal structures of the wind field on the basin-scale internal wave spectrum in Lake Iseo. This deep Italian basin is characterized by the presence of a large island, imparting attributes of an annulus to the lake. During the summer of 2010, the internal wave activity was dominated by a basin-scale internal wave of vertical and horizontal modes 1 (V1H1), superimposed on which were occasional higher vertical modes (V2H1) and higher horizontal modes (V1H5) trapped by the main island. The occurrence of these motions was interpreted as forcing by the wind components with similar horizontal structures and with energies at frequencies near the natural oscillations of the excited modes. The modifications of the wind field by the topography, in particular, controlled the excitation of an anticyclonic wave trapped around the island, whose features were investigated on the basis of an extension of the circular model to the case of an annular basin of constant depth.

The water column in a stratified lake responds to surface wind forcing similarly to a three-dimensional mechanical, viscously damped oscillator, exhibiting a spectrum of oscillatory modes with characteristic periods and spatial structures. These modes are eigenmodes of the stratified water body with a structure that depends on the size and shape of the lake basin and the details of the density distribution (Mortimer 1974; Imberger 1998). Particular modes are excited during a wind disturbance depending on the frequency and spatial distribution of the applied wind force (Mortimer 1953; Antenucci and Imberger 2003).

Mortimer (1952) provided the first conceptual model for the study of the basin-scale internal waves in lakes by approximation of water column stratification into two, three, or more layers. For such a step structure idealization, the modal structures and their response to wind forcing have been determined for progressively more complicated cases, beginning with the equivalent depth models (Bäuerle 1985), this being extended to take into account real bathymetries (Wang et al. 2000; Lemmin et al. 2005; Shimizu et al. 2007), weakly dissipative systems (Shimizu and Imberger 2008), and nonlinear and weak non-hydrostatic effects (de la Fuente et al. 2008). These authors showed that the details of the layered structure play a critical role in determining the period of the individual modes (Mortimer 1952), the internal wave amplitude and phase relative to the wind under forced conditions (Antenucci et al. 2000), the vertical structure of the velocity field (Forcat et al. 2011), as well as the time scales for nonlinear wave steepening (Horn et al. 2001).

For the simple case of a rotating flat-bottomed circular or elliptical basin, sectioning the water column into discrete-density inviscid layers allows analytic solutions for the horizontal structure of the basin-scale internal waves and the associated dispersion relationship (Antenucci and Imberger 2001). The key nondimensional number, determining the wave characteristics, is the ratio of the time the basin takes to rotate to the period of the internal wave mode oscillation, called the Burger number (S), defined as:

$$S = \frac{c}{fL} \tag{1}$$

where c is the non-rotational baroclinic phase speed, f the inertial frequency, and L the horizontal length scale of the basin. As the Burger number approaches zero, the structure of the internal waves may be visualized in terms of fundamental cyclonic Kelvin and anticyclonic Poincaré wave modes, the former being confined to the boundary with an amplitude exponentially decreasing offshore and with an equal partitioning between potential and kinetic energy, and the latter being localized more in the lake interior with a frequency approaching the inertial frequency and with the majority of energy being kinetic. With increasing Burger number, the cyclonic waves become super-inertial and their horizontal structures approach that of the anticyclonic wave. Antenucci and Imberger (2001) derived the analytical solutions for waves in an elliptical basin and showed that the interfacial displacement was greatest at the antinodes on the major axis of the ellipse where the radius of curvature was smallest, in agreement with the earlier numerical results of Schwab (1977) and the later numerical verification of Gomez-Giraldo et al. (2006).

The influence of increasing basin complexity on internal wave structure has often been explored with the aid of three-dimensional models. Nonuniform bottom bathymetry may dramatically modify the spatial structure of natural modes, by amplifying the wave velocities over sloping bottoms (Fricker and Nepf 2000; Gomez-Giraldo et al. 2006) and magnifying velocities and wave amplitudes over

* Corresponding author: giulia.valerio@ing.unibs.it

local bathymetric features. This phenomenon, known as ''wave trapping,'' has been observed for specific Poincaré-type modes (Bäuerle 1994; Wang et al. 2000). Besides the bathymetry, embayments may also modify the Poincaré-type structure, introducing accompanying cyclonic cells (Gomez-Giraldo et al. 2006); further, they may generate subbasin oscillations and increase the integrated kinetic energy oscillations where the boundary is convex (Rueda et al. 2003). Accordingly, the amplification of the interfacial displacement described by the analytical solutions in elliptic basins is a special case of embayments supporting local trapped internal waves well known from numerical solutions of lakes with complicated geometry (Rueda et al. 2003; Okely et al. 2010). The presence of islands in lakes may also cause the generation of upwelling and downwelling zones (Chubarenko et al. 2001) or induce vortices generated by a lee-side separation of wind field interacting with a three-dimensional topographical obstacle (Rueda et al. 2005). Further, Kodomari (1984) showed, numerically, that the presence of an island in a lake basin may increase the period of the superficial seiche; the effects of islands on the horizontal structures of the internal waves does not appear to have been investigated.

A wind stress on the surface of a lake will do work on the lake's water column if the water is moving in the same direction as the wind stress, and conversely the water column will do work on the wind field if the drag and water move in opposite directions. Clearly, therefore, the closer a wind field is matched in horizontal structure and frequency to the surface velocity of the water motion in a lake, the more effectively will the wind impart energy to the lake and the more rapidly will the internal motions in the lake intensify (Antenucci and Imberger 2003). Accordingly, the occurrence of particular wave modes depends on the relationship between the temporal and spatial structures of the wind forcing and the natural modes; resonance is achieved when the wind period approaches the natural free mode period and when the phase shift between the wind forcing and the surface water velocity due to the internal wave is zero (Mortimer 1953; Antenucci et al. 2000; Rueda et al. 2003). The spatial structure of the wind field thus plays a critical role in the excitation of higher horizontal modes (Wang et al. 2000; Lemmin et al. 2005; Okely et al. 2010), transversal seiches (Roget et al. 1997), as well as for the generation of direct, large-scale circulation patterns like the stationary gyres localized in lakes' surface layer (Strub and Powell 1986; Laval et al. 2003; Marti and Imberger 2008). This is of particular relevance in mountainous terrain, where the topography surrounding a basin may strongly modify the spatial structure of the mesoscale or even synoptic wind events (Lemmin and D'Adamo 1996), including sheltering effects or flow separations (Rueda et al. 2005).

In this paper we present the structure of basin-scale internal waves in Lake Iseo, a subalpine lake in the north of Italy, which has a large island located in the middle of the basin imparting an annulus-like shape to the lake, in response to lake bathymetry and wind spatial and temporal distribution. To the best of our knowledge, this is the first study that investigates the internal hydrodynamics of Lake Iseo.

The remainder of the paper is organized as follows. First, we describe the study site, the field equipment, and the numerical model, including an argument about the importance of the choice of the layered structure and the wind field for the simulation of the internal wave activity. Then we present the numerical results and their comparison with a detailed field data set, collected during an experimental campaign undertaken during the stratified period, and we highlight the influence of spatial and temporal scale of the wind on modes excitation. Finally, we discuss the role of the peculiar Lake Iseo bathymetry on the internal wave motions by analyzing the influence of the island on the wave structure and developing a simplified theoretical solution for its interpretation.

Methods

Field site—Lake Iseo is a deep Italian lake located in the pre-alpine area of east-central Lombardy at the southern end of a wide valley, Valle Camonica. On the south it is open to plain, while high mountains and several lateral valleys are present on both the eastern and western sides.

The wind field is deeply influenced by the surrounding topography, generating a variety of thermally and dynamically driven wind systems, settable in the classical theory of valley winds well documented for this geographical area (Defant 1951; de Franceschi et al. 2002). Under ordinary meteorological conditions, two main winds blow along the thalweg: the northerly ''Vet'' during the night and the southerly ''Ora'' during the afternoon (Fappani 2005).

Covering a surface area of 60.9 km^2, the lake has a maximum depth of 256 m and is characterized by an annular bathymetry, as shown in Fig. 1. The large, centrally located island, Monte Isola, covers an area of about 4.5 km^2 and has a peak elevation of 415 m above the lake surface, presenting a major obstacle for the wind field.

The lake bathymetry may be synthetically described through five main physiographical units (Bini et al. 2007): (1) the irregular southward-dipping Oglio prodelta in the northern part of the lake; (2) a central basin with a regular flat floor between 240 and 256 m in depth; (3) the Monte Isola submerged escarpment, located at the western side of Monte Isola and emerging at the small islands of San Paolo and Loreto; (4) the Sale Marasino plateau, with a maximum depth of 100 m, between Monte Isola and the eastern shore of the lake; and (5) the southern Sarnico basin, irregularly shaped and rising westwards, where the Oglio River exits from the basin.

Field data—The present study used wind speed and direction and water temperature data collected in the locations shown in Fig. 1, during the period 13 July to 02 September 2010, including an intensive field campaign from 13 to 28 July 2010. The field equipment consisted of a Lake Diagnostic System (LDS) (Imberger 2004) moored on December 2009 in the northern part of the lake, three additional thermistor chains (TC), and four wind stations (WS1–WS4) deployed on the lake shore during the experimental period, integrated with three wind stations

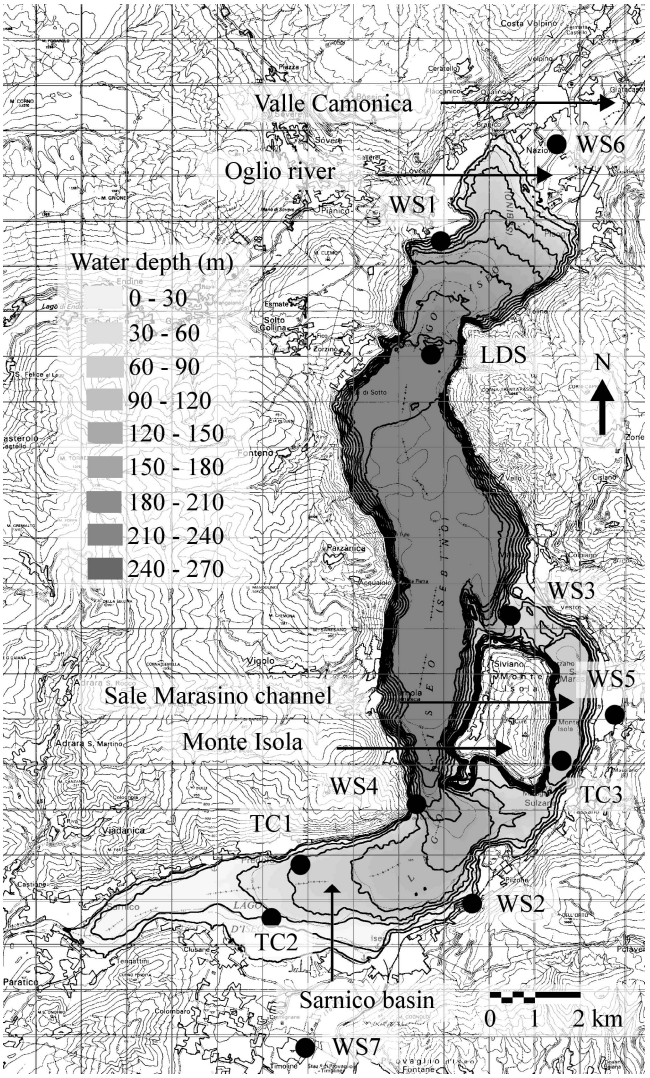

Fig. 1. Bathymetry of Lake Iseo, represented with isodepth lines at 30-m spacing, and location of the measurement stations: thermistor chains (TC), wind stations (WS), and lake diagnostic system (LDS). The coordinates for the location in the bottom-left corner of the map are 45.63°N, 9.94°E. (Bathymetric data source: Regione Lombardia.)

already present in the surrounding area (WS5–WS7). Station deployment details are summarized in Table 1.

The LDS consisted of meteorological sensors (wind speed and direction, net total radiation, incoming short wave radiation, air temperature, and relative humidity) located at 2-m height above the water surface and a thermistor chain, 50 m long and equipped with 21 underwater sensors measuring water temperature at different depths that varied from 0.25 to 49.75 m. The submerged thermistor chains TC1 and TC2 monitored the first 36 m of the water column in the southern basin with 16 and 18 sensors, respectively. With accuracy ± 0.01°C, these thermistors were fixed at depths assuring the maximum spatial resolution around the thermocline during the stratified season. Finally, located close to the main island shore, TC3 was equipped with two sensors measuring at depths of 10 and 15 m water temperature fluctuations to ± 0.002°C.

Numerical model—The objective of this paper was to determine the spatial structures of basin-scale internal waves in Lake Iseo in response to lake bathymetry and wind spatial and temporal distribution during the stratified period. Accordingly, the focus was on understanding a few isolated wind forcing events documented during the field experiment, so that the density profile of the water column could be assumed constant in time and subdivided into a finite number m of vertical layers, stacked vertically, each with a uniform density.

Mathematically, the conservation equations that govern the motion of this layered system may be described by $3m$ scalar partial differential equations that express the mass and momentum balance in the rotating frame of reference on the basis of the linear, hydrostatic, Boussinesq, and layer approximation (Platzman 1972), retaining as dependent variables the layer-averaged horizontal velocity $\vec{v}_k$ and the interface displacement η_k of each layer k.

The assumption of a simple harmonic dependence with exponential decay on time t of the state vector of motion:

$$\xi(\vec{x},k,t) = [\eta_1 \quad \eta_2 \quad \dots \quad \eta_m \quad \vec{v}_1 \quad \vec{v}_2 \quad \dots \quad \vec{v}_m] \quad (2)$$

reduces the solution of the free baroclinic oscillations to an eigenvalue problem that provides a set of angular frequencies of oscillation $\omega^{(q)}$ and damping rates $\gamma^{(q)}$ with their corresponding right eigenvector $\tilde{\xi}^{(q)}(\vec{x},k)$. Each eigenvector represents the amplitude of the layer velocities and interface displacements as a function of the horizontal coordinates $\vec{x} = [x \quad y]$, thus representing the spatial structure of a dissipative horizontal normal mode q associated with a particular frequency $\omega^{(q)}$ and a damping rate $\gamma^{(q)}$. Which of these natural modes are brought into play during any particular disturbance depends on the period and the spatial distribution of the applied force. In order to quantify the effect of a certain wind stress distribution $\vec{\tau}$ on each mode, Shimizu et al. (2007) derived the decoupled evolutionary equations for each mode q, taking advantage of the completeness and orthogonality properties of modes. Through the numerical solution of first-order differential equations as a function of time only, it is therefore possible to derive the temporal evolution of the modal amplitude $\tilde{a}^{(q)}$, phase $\Phi^{(q)}$, and energy $E^{(q)}$ (*see* Shimizu and Imberger 2008 for details). For a better understanding of the following results, it is important to recall, in particular, the equation:

$$\frac{\partial}{\partial t} E^{(q)}(t) = \dot{W}^{(q)}(t) - \dot{D}^{(q)}(t) \quad (3)$$

that relates the modal energy to the modal rate of working by wind:

$$\dot{W}^{(q)}(t) = \int_A \left(\vec{v}_1{}^{(q)*} \times \vec{\tau}\right) dA \quad (4)$$

Table 1. Details of the deployments of the measurement stations.

Sta.	Deployment period	Sampling interval (s)	No. and location of thermistors
LDS	05 Dec 2009–present	10	21, from 0.25 m to 50 m
TC1	10 Apr 2010–present	20	16, from 4 m to 36 m
TC2	12–28 Jul 2010	10	18, from 1 m to 33 m
TC3	31 Jul 2010–02 Sep 2010	10	2, at 10 m and to 15 m
WS1	19 May 2010–present	60	
WS2	19 May 2010–present	60	
WS3	10–28 Jul 2010	30	
WS4	10–18 Jul 2010	30	
WS5	16 Nov 1995–01 Aug 2010	3600	
WS6	26 Jul 1993–present	3600	
WS7	10 Sep 2008–present	3600	

and the modal rate of energy dissipation:

$$\dot{D}^{(q)}(t) = 2\gamma^{(q)} E^{(q)}(t) \tag{5}$$

where the superscript * denotes the complex conjugate and A is the surface area of the basin. $\dot{W}^{(q)}$ expresses the efficiency of the wind in energizing the mode q: when it is positive, the wind works on that mode; this energy transfer becomes larger as the water and wind vectors converge in space and time. In contrast, an opposing stress and velocity lead to negative value for the rate of work, which may be interpreted as the water working on the wind field (de la Fuente et al. 2008). This explains why energy fluxes tend to be channeled in the wave motions that match the temporal and spatial distributions of surface stress. Solutions of Eq. 3 were used, below, to calculate the individual energetic contribution of each mode with respect to the lake motion as a whole.

Model setup—In order to interpret the internal wave structure observed in Lake Iseo, simulations were conducted using the modal model developed by Shimizu et al. (2007) for the period of the field experiment (13–28 July 2010). The bathymetry of the lake was discretized with a 160×160-m horizontal grid and the time step was set equal to 900 s. Energy dissipation by bottom friction was included in the model through a linear bottom friction coefficient c_b (Shimizu and Imberger 2008); its dimensionless value, 10^{-2}, was obtained by matching the wave amplitudes measured at LDS location during October 2009. Water temperature data during the study period indicated that the water column might be divided into a well-mixed and warm surface layer, separated from the relatively stagnant and uniformly cold hypolimnion by an intermediate metalimnion. The upper interface of the metalimnion was well defined by an abrupt jump in temperature, while the lower interface was somewhat arbitrary because of the gradual reduction of the temperature gradient. A reduction of approximately 0.005 Hz in the Brunt–Väisälä frequency might be identified around the depth of 30 m, and so this depth was assumed as the upper interface of the hypolimnion. On the basis of these criteria, the layer properties were calculated from the temperature profiles measured continuously by the LDS. Density stratification evolved during the experiment. Some cooling–warming phases affected the surface layer and an abrupt deepening event of the thermocline occurred after the first week (*see* Fig. 2). However, for the majority of the simulation period, the average profile reproduced well the main features of the thermal stratification; accordingly, the layered structure was assumed constant within the simulation and calculated on the basis of the average vertical profile (*see* Table 2).

The sensitivity of the model to variations of the layered structure was tested, showing that the thickness of the upper layer most strongly influenced the internal wave period of the first vertical mode, and the metalimnion thickness had a strong influence on the second vertical mode periods. This is consistent with what is reported in the literature (Mortimer 1952; Horn et al. 1986; Münnich et al. 1992). The thickness of the upper layer has been found to be particularly critical in determining the wave response under forced conditions in Lake Iseo because the typical wave response always contained most of the energy in the vertical and horizontal mode 1 (V1H1). Accordingly, care was needed to match the density distribution so that the fundamental period was correct; otherwise, the observed resonance was not reproduced by the model. On the contrary, the location of the lower interface was found to more weakly affect the simulation results.

Moreover, the layered structure controls the rate of wave steepening (wave shape) in deep lakes, as shown by Horn et al. (2001), who introduced the steepening time scale for a two-layer system of depth h_1 over depth h_2 as

$$T_s = \frac{T_i}{3\eta_0 \dfrac{h_2 + h_1}{h_1 h_2}} \tag{6}$$

which defines when the nonlinear effects become important for free oscillation of initial amplitude η_0 and period T_i, and the consequent degeneration of basin-scale internal wave into solitons. For a strong interfacial perturbation, vertical accelerations were expected to significantly influence the wave structure in Lake Iseo, due to the small ratio of the thermocline depth to the overall depth of the lake. However, under forced conditions the ratio between the time scale T_s and the dominant wave period T_i was small, so that there was not enough time for the waves to steepen before the available energy was again extracted by the wind. For this reason, under ordinary conditions the basin-scale motions

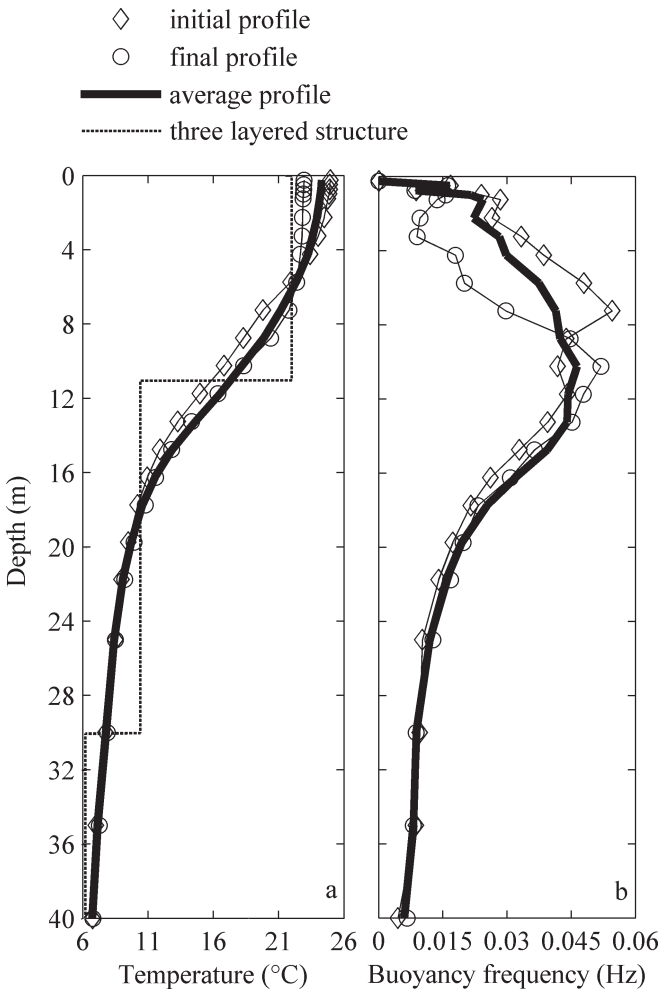

Fig. 2. Vertical profiles of (a) temperature and (b) buoyancy frequency obtained from the temperature data measured at the LDS location and averaged over the periods: 13–16 July 2010 (initial profile); 25–28 July 2010 (final profile); and 13–28 July 2010 (average profile). The three-layered structure imposed as the initial condition in the July simulations (*see* Table 2) is also shown.

retained many of the characteristics of linear waves and a linear model was capable of capturing the main structural features of the excited basin-scale waves.

Results

The two-dimensional wind field—During the field experiment, the eight wind stations installed in the lake area (*see* Fig. 1) provided data for the temporal and spatial patterns of the surface stress field acting on Lake Iseo.

The Vet and the Ora winds were described by the signals measured in the two on-lake wind stations (LDS and WS3) and in the land-based stations located in open areas far enough from the influence of the perimeter topography (WS6 and WS7). The wind measured on the lake shore close to mountainsides (WS1, WS2, WS4, WS5) exhibited an additional down-slope component (Fappani 2005). Figure 3 highlights the considerable spatial variability of the wind field induced by the topography, the narrow Sale Marasino channel on the east side and the southwestern Sarnico basin being sheltered from the prevailing winds, and relevant inhomogeneities being observed between wind intensities measured in lateral coastal and on-lake areas. For wind directions, the rose diagrams clearly show the effect of aerodynamic modifications induced by the surrounding topography, due mainly to the funneling of the airflow into the valley and the generation of local down-slope directed breezes in the shore–lake transition.

Three-dimensional modeling of the temperature field of Lake Iseo during the experimental period, carried out with the hydrodynamic model ELCOM (Hodges et al. 2000), showed that an overestimate of surface layer deepening resulted in the southern basin when the wind measured at the LDS location was assumed uniformly distributed on the whole lake. Accordingly, simulations were carried out with spatially varying wind fields. A temporally–spatially varying wind field was first constructed using a bilinear interpolation (Laval et al. 2003) of the wind components measured at the eight wind stations, all linearly interpolated on a time interval of 15 min. The ELCOM results were used to refine the spatial variations of wind in order to produce the correct vertical mixing, especially in the southern basin. This refinement was obtained by copying existing wind data to other locations, as shown in Fig. 4. A full two-dimensional wind field, referred to as IWF hereafter, was constructed including both real and "ghost" stations in the wind interpolations and used to numerically simulate the basin-scale internal waves in Lake Iseo. To highlight the role of spatial variability of the forcing, these numerical results have also been compared with those obtained by imposing a uniform wind over the whole lake, referred to as UWF, using the wind data measured at the LDS location.

The main temporal and spatial features of the IWF were expressed by the vector horizontally averaged wind stress, curl, and divergence (Laval et al. 2003; Rueda et al. 2005). The average wind stress (*see* Fig. 5a) had a pronounced daily periodicity due to the cycle of a nightly northerly wind

Table 2. Characteristics of the three-layered structure imposed as the initial condition in the simulations. z_k represents the depth of the upper interface of the layer k and T_k the layer temperature.

	Depth of the upper interface, z_k (m)		Water temperature, T_k (°C)	
Layer, k	13–28 Jul 2010	01–15 Aug 2010	13–28 Jul 2010	01–15 Aug 2010
1	0	0	22.3	21.4
2	11.0	12.0	10.7	10.6
3	30.0	30.0	6.5	6.5

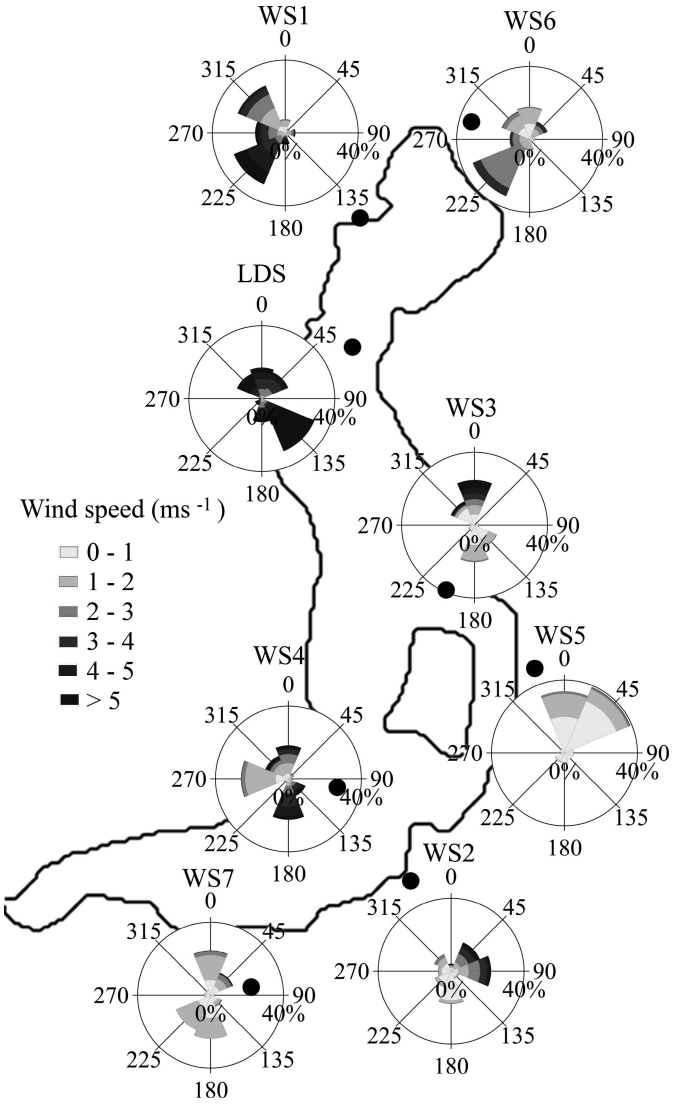

Fig. 3. Rose diagrams related to the wind field measured by the wind stations (marked with black dots) near Lake Iseo in the period 13–28 July 2010. In a polar coordinate system, these diagrams indicate the relative frequency, proportional to the length of each spoke, of the winds blowing from a certain direction; the shade-coded bands indicate the velocity range to which the wind belongs.

and an afternoon southerly wind discussed above, the southerly one typically being more intense. During the experimental period, two exceptional events interrupted this regular temporal pattern: a strong storm on 18 July 2010 and a long-lasting northerly wind continuing for more than a day around 24 July 2010 (*see* Fig. 5a). Regarding the spatial scales, the interpolated wind field was characterized by an average negative curl and divergence during the afternoon (*see* Fig. 5b,c). In order to clarify this aspect, in Fig. 4 two snapshots have been selected from the IWF as being representative of the typical (a) night and (b) day conditions. The following spatial features may be observed: (1) Two main uniform areas, the central basin and the southern Sarnico basin, the latter presenting a reduced

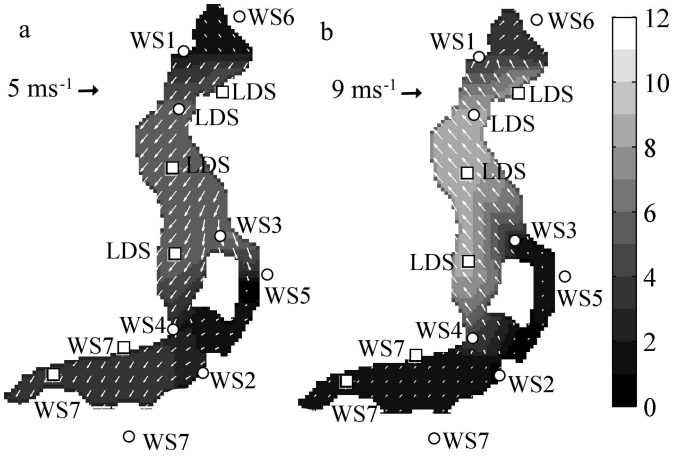

Fig. 4. Spatially varying wind field (IWF) obtained by interpolating the wind station data (a) at 04:10 h on 17 July 2010, representative of a typical nighttime wind pattern; and (b) at 12:10 h on 17 July 2010, representative of a typical daytime wind pattern. The shading refers to wind speed (m s^{-1}) while the arrows indicate the wind velocity vectors. Circles indicate real wind stations, while squares indicate the corresponding ghost stations included for the generation of the wind field.

momentum with respect to the former. This difference was a consequence of the extrapolation of the LDS and WS7 data in the central and southern basin, respectively. The reduction of wind speeds in the southern part is particularly pronounced in Fig. 4b (i.e., during the day), justifying the maximum of the average wind stress divergence around noon; (2) the sheltering of the eastern Sale Marasino channel and the leeward area by Monte Isola, obtained through the interpolation of WS2, WS3, and WS5 data; (3) a marked deviation of wind direction easterly (westerly) in the central (northern) part of the basin, caused by the funneling effect of the valley during the day. This feature, obtained through the interpolation of WS1 and WS6 data, justifies the negative average curl of the wind stress observed around noon; and (4) a strong reduction in the wind speed in the northern basin, probably due to the WS1 and WS6 underestimation of the on-lake wind speed.

Characteristics of the free basin-scale internal waves—In order to investigate the internal wave response to wind forcing, it was helpful to first determine the free basin-scale modes and their characteristics for the three-layered model described in Table 2. Without any external forcing, the solution of an eigenvalue problem provided mode types and periods, summarized in Table 3, and the associated spatial distribution of layer velocities and interface displacements $\vec{\xi}^{(q)}(\vec{x},k)$. Their horizontal structures are shown in Fig. 6 with reference to the first vertical mode; in the next sections the analysis will address their vertical structure. Horizontal mode H1 was a Kelvin wave rotating cyclonically (counterclockwise) around the basin with a period close to 24 h. The velocities were seen to be tangential to the lake boundaries and are directed southerly for half the period and northerly for the other half. The velocity field showed maximum and minimum speeds, respectively, in the central part of the basin and at the two

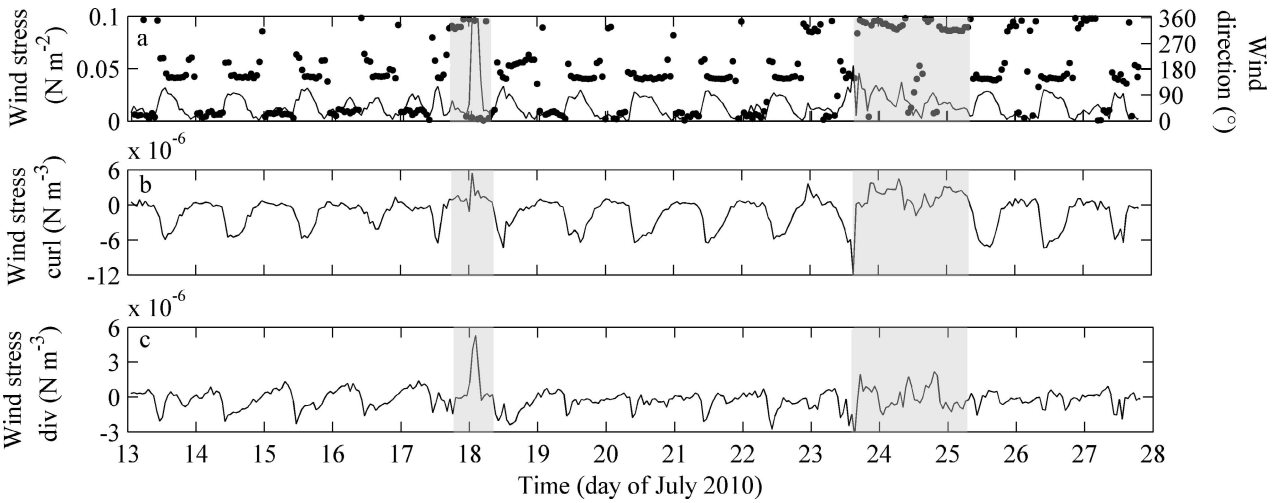

Fig. 5. Record of vector horizontally averaged wind measurements over Lake Iseo during the field experiment: (a) average wind speed (solid line) and direction (dots), (b) curl of wind stress, and (c) divergence (div) of wind stress. Gray-shaded areas mark two wind events of particular relevance.

antinodes located in the northern and the southern parts of the basin. The next four horizontal modes presented a multicellular structure, characterized by elliptical or circular-shaped cells around each antinode that may be considered to oscillate separately, as commonly assumed in multi-basin lakes (Stocker et al. 1987). It is noteworthy that mode H2 presented maximum layer velocities in the areas around the two main regions where the radius of curvature of the perimeter is smallest, while in H3 and H5 the epilimnetic velocities became strongly amplified in the southern basin and around the main island, respectively. All the cells rotated cyclonically (counterclockwise) with sub-daily periods in the range 7–15 h, except for the one attached to Monte Isola, the fifth horizontal mode that rotated clockwise around the island.

Comparison between wind stress and free modes structure—As discussed in previous sections, the energy fluxes tend to be channeled into the wave motions that have surface velocity field that match the temporal and spatial distributions of the surface wind stress. To highlight this phenomenon, synthetic wind fields were constructed from the temporal and spatial structure of the first five modal surface velocity fields. These were applied to Lake Iseo, and their effects on the wave motions were quantified through the modal rate of working $\dot{W}^{(q)}$ (*see* Eq. 4). As shown in Table 4, for internal vertical mode 1, wind modes excited only matching internal wave modes. Besides, given a certain spatial wind distribution, the time scale controlled the relative excitation of higher modes. This is shown in Table 5, where results refer to wind fields sinusoidal in time and uniformly distributed over the lake. Resonance between wind and internal waves was achieved under the forcing with a period closer to the mode period; in such a case, the maximum relative contribution of the matching mode occurred.

Table 3. Types and periods of the modes under analysis, for the two periods of simulation.

Simulation period	Wave period (h)					
	V1H1	V1H2	V1H3	V1H4	V1H5	V2H1
13–28 Jul 2010	24.5	14.5	9.6	7.7	7.1	56.4
01–15 Aug 2010	24.4	14.2	9.5	7.4	7.0	59.4

The analysis of these simplified cases allowed us to draw some general conclusions. The dominant daily periodicity of the IWF was close to the 24.5-h natural period of the V1H1 mode. Also, V1H1 surface velocity field (*see* V1H1 in Fig. 6) was the one that best reproduced the wind stress distribution (*see* Fig. 4), both characterized by higher speeds in the central part of the lake and by vectors directed along the lake axis, following the valley morphology, all uniformly southbound or northbound depending on the phase. This spatial fit was clearly shown by the cross-correlation function calculated between the modal velocity structure and the IWF, everywhere positive and maximized when V1H1 mode is concerned (*see* Fig. 7). Hence, V1H1 was the mode that captured most of the wind energy. An analogous spatial fit existed between the wind stress distribution and the velocity structure of the higher vertical modes having an H1 structure. However, since they were characterized by lower frequencies, they were expected to be favored by occasional long-lasting wind events.

With regard to the higher horizontal modes, the coexistence of area characterized by positive and negative correlation with the wind (*see* Fig. 7), due to the changes in the velocity directions among the nodes of the system, suggested that their contribution was strongly reduced with respect to V1H1. However, some similarities also existed between the spatial structure of the IWF (*see* Fig. 4) and the upper velocities of the second (*see* V1H2 in Fig. 6) and fifth (*see* V1H5 in Fig. 6) horizontal modes. V1H2 and the wind field had in common higher speeds in the northern part of the lake with respect to the southern one, while IWF

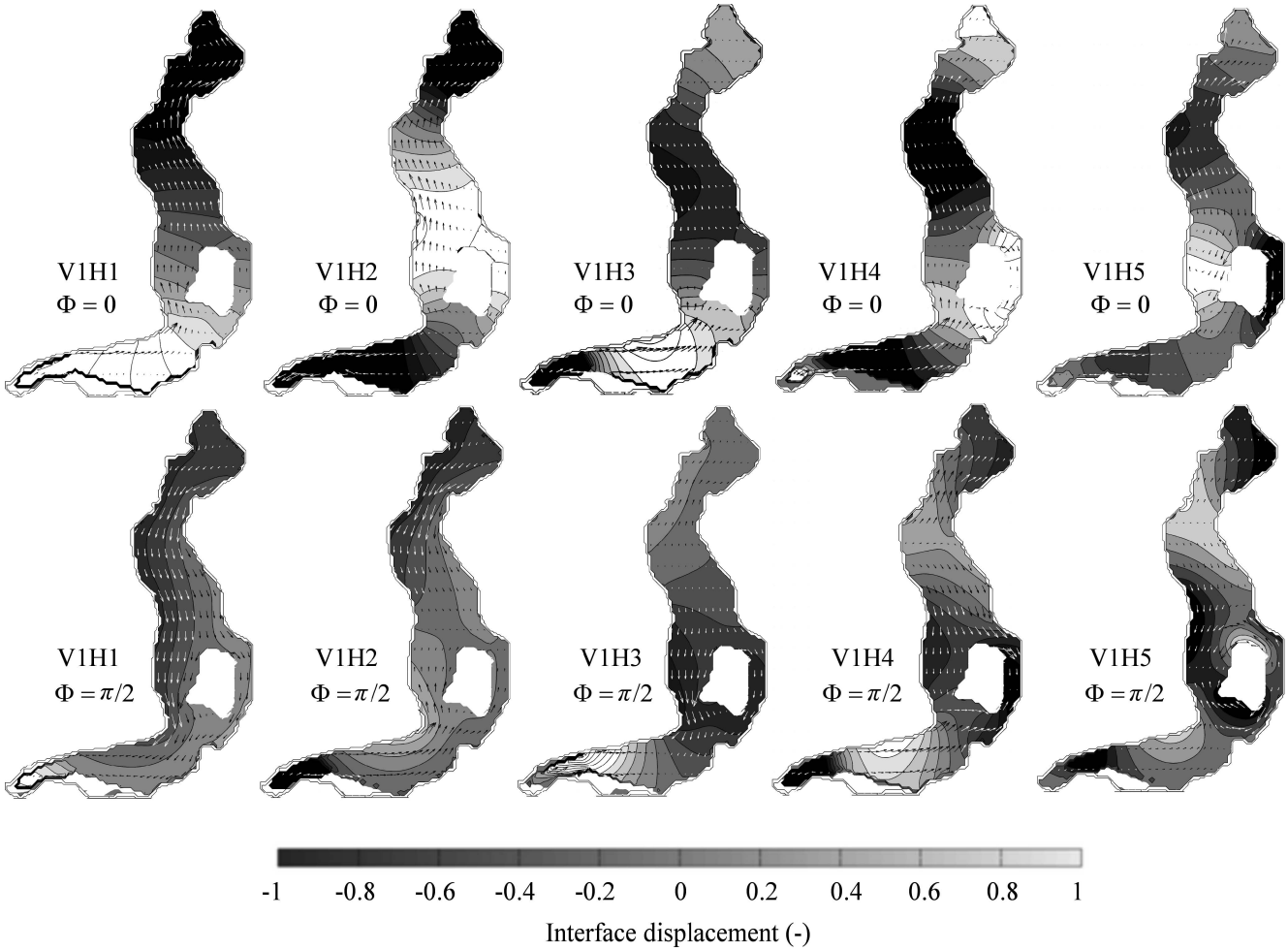

Fig. 6. Representation of the horizontal modes (from V1H1 to V1H5) of Lake Iseo calculated with a three-layer model representing the average stratification of water column during the field experiment. The shading represents the nondimensional vertical displacements $\eta : \eta_{max}$ of the second layer upper interface with respect to its equilibrium level. The arrows indicate the average velocities of the upper layer and Φ is the phase.

structure presented a nonuniform distribution of the velocities around the island, which was the prominent feature of the velocity field of the fifth mode. This spatial fit thus also favored the excitation of these wave motions. This clearly appeared from the analysis of the splitting of energy among modes under simplified steady wind fields: the integral rate of work by the Ora wind field represented in Fig. 4b on mode V1H2 and V1H5 was maximized (6.1% and 1.3%, respectively) when compared with the case of a southerly (SN) wind uniformly distributed on the whole lake (0.09% and 0.03%, respectively).

Table 4. Splitting among the first five horizontal modes of the maximum integral rate of work by five wind fields characterized by the same temporal and spatial structure of these modes. The maximum contribution under a certain wind is shown in bold.

	Wave (%)				
Wind	V1H1	V1H2	V1H3	V1H4	V1H5
V1H1	**99.98**	0.02	0.00	0.00	0.00
V1H2	0.07	**99.90**	0.02	0.00	0.00
V1H3	0.04	0.15	**99.66**	0.10	0.06
V1H4	0.01	0.04	0.69	**95.04**	4.22
V1H5	0.00	0.01	0.05	0.62	**99.32**

Observed basin-scale internal wave activity—Temperature measurements recorded in the period 13–28 July 2010 at stations LDS, TC1, and TC2 were analyzed in order to determine the temporal and spatial patterns of the basin-scale internal wave response. The time series of the isotherm depths, calculated by linear interpolation from the temperature data, are shown in Fig. 8a–c; the diurnal periodicity of the V1H1 mode is clearly visible. The vertical displacements of the two southern chains (TC1 and TC2) were almost coincident, while the response at the northern station at the same depth occurred in counter phase, suggesting a horizontal H1 structure. The coherence and phase of the 20°C isotherm at the LDS and TC1 locations is shown in Fig. 9a, where it is seen that at 24 h the peak in coherence was close to 1 and phase was equal to about

Table 5. Splitting among modes of the maximum integral rate of work by sinusoidal wind fields, uniformly distributed over the lake and characterized by different wave periods. The maximum relative contribution of each mode is shown in bold.

	Wave period (h), %									
Wind period (h)	V1H5 (7)	V1H4 (7.7)	V1H3 (9.6)	V2H5 (12.6)	V1H2 (14.5)	V2H4 (15.8)	V2H3 (19)	V1H1 (24.5)	V2H2 (31.6)	V2H1 (56.4)
6	**3.16**	**1.35**	0.59	0.06	0.29	1.23	0.83	89.70	1.37	1.42
9	0.80	1.30	**5.37**	0.12	0.43	1.62	0.92	87.01	1.23	1.19
12	0.13	0.18	0.67	**0.56**	**1.13**	**2.49**	1.16	91.51	1.15	1.01
18	0.01	0.02	0.03	0.02	0.24	0.98	**2.32**	95.19	0.72	0.46
24	0.00	0.00	0.00	0.00	0.01	0.05	0.11	**99.43**	0.29	0.10
36	0.01	0.01	0.01	0.00	0.04	0.20	0.27	91.45	**5.19**	2.82
48	0.01	0.01	0.02	0.01	0.05	0.26	0.31	77.90	3.06	18.38
60	0.01	0.02	0.02	0.01	0.05	0.26	0.30	67.28	2.25	**29.80**

170°, confirming that the two T-chain stations were located close to the antinodes of the oscillatory system. Regarding the vertical structure of the oscillations, it is evident from Fig. 8 that the daily isotherm motion, at all stations, appeared mainly in phase over the different depths, indicating that most of the motion had a vertical mode 1 structure.

In order to investigate the excitation of the second vertical modes, the metalimnion thickness was calculated as the distance between the 8°C and the 18°C isotherms. A spectral analysis of the energy content of the metalimnetic thickness at the LDS and TC1 (Fig. 9c) highlighted a significant coherence in correspondence of 2.5-d period, suggesting the existence of a second vertical mode oscillation superimposed on the fundamental mode. This lower frequency oscillation might be quite clearly identified by low-pass filtering the signal with a cutoff period of 2 d. The resulting filtered signal, shown as a function of time in Fig. 10, highlighted the presence of the low-frequency oscillation of the metalimnion thickness that occurred in counter phase at the northern and southern T-chains. This motion was significantly amplified by the end of the observation period.

A thermistor chain (TC3) was installed close to the island shore from 31 July to 02 September 2010 (*see* Fig. 1) to monitor the water temperature oscillations close to the island. Figure 11a presents the spectra of water temperature measured at 10 m below the surface, comparing the northern and southern thermistor chains (LDS and TC1) with the one close to the island (TC3). The LDS and TC1 data did not show a peak of energy for sub-daily frequencies, but a statistically significant peak with a period of about 7 h is clearly visible in the TC3 spectrum. Evidence of the local occurrence of higher horizontal modes close to the island may also be found in the time series of the temperature signal shown in Fig. 12a. At the TC3 location a daily V1H1 fluctuation, out of phase with respect to the LDS signal, was superimposed on a higher frequency oscillation characterized by a V1-type structure that became dominant at the times shown by the gray shading in Fig. 12.

Simulated and observed basin-scale internal wave activity—The observed V1 nature of the isotherm deflections allowed a simple comparison between the simulated and measured data via the specific potential energy fluctuations in the first 50 m of the water column (Fig. 13). The overall results agreed well with the field data, in both amplitude and phase. Some discrepancies might be observed in the southern basin, where the model underestimated the wave downwelling that followed the events of 18 July 2010 and 24 July 2010 and also showed a small phase delay between the minima in the second half of the simulation.

The energetics of the wave excitation are shown in Fig. 14, which reports the partitioning of the total energy, as defined by Eq. 3, between the different contributing

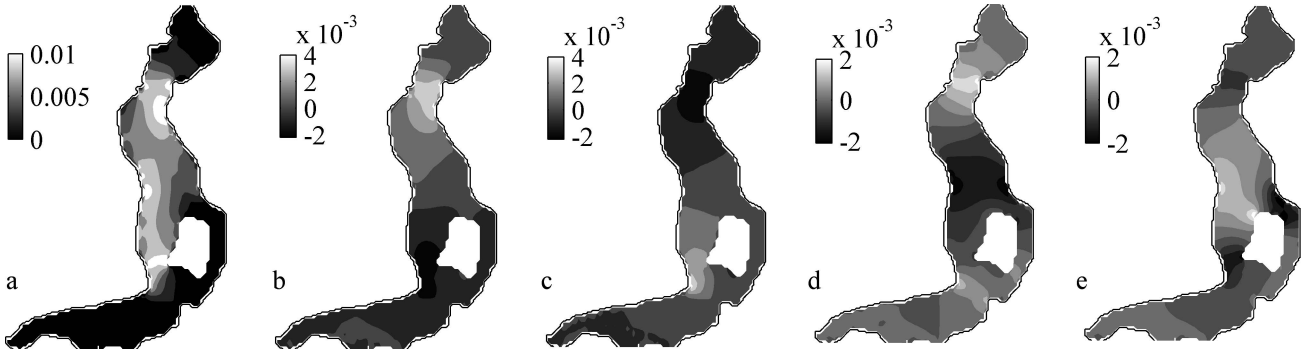

Fig. 7. Contour maps showing the cross-correlation function calculated between the SN component of the IWF and the upper layer velocities of mode (a) V1H1, (b) V1H2, (c) V1H3, (d) V1H4, and (e) V1H5.

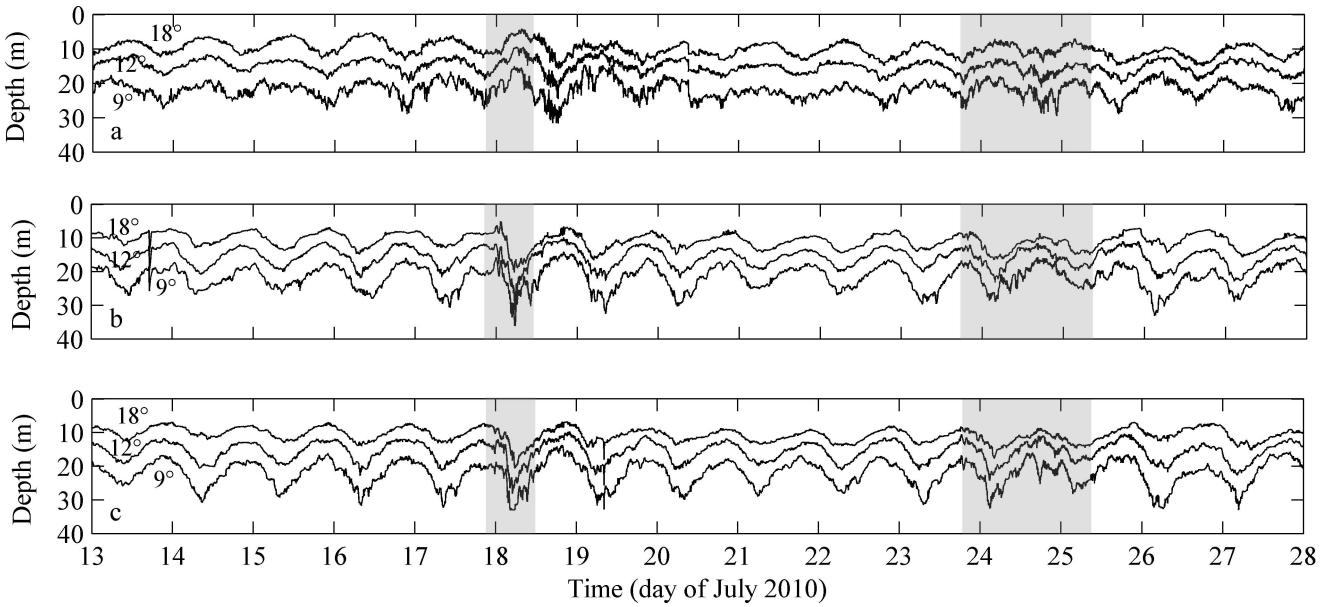

Fig. 8. Time series of the vertical displacements of the 9°C, 12°C, and 18°C isotherms recorded at (a) LDS, (b) TC1, and (c) TC2 locations. Gray-shaded areas mark the internal wave response corresponding to two wind events of particular relevance.

modes. Figure 14 also includes a comparison of the simulated energy partitioning obtained using the IWF and the UWF as a boundary condition, aimed to clarify the role of the wind structure on basin-scale internal wave motions in Lake Iseo. During the period under consideration, mode V1H1 was, as expected from above, the dominant internal wave motion excited by the forcing. Indeed, Fig. 14a shows that the fundamental mode contained $> 90\%$ of the wind rate of working, coherently with the wind–wave coupling at a daily period indicated by measurements (*see* Fig. 9b). As shown in Fig. 14b, the other modes generally played a minor role, each individually providing no more than about 3% of the total energy during the period of investigation.

Consistent with the field data, a relevant transfer of wind energy to the V2H1 mode was simulated by the model after the long-lasting moderate wind event of 24 July 2010 (*see* Fig. 14b). This V2H1 motion was associated with an

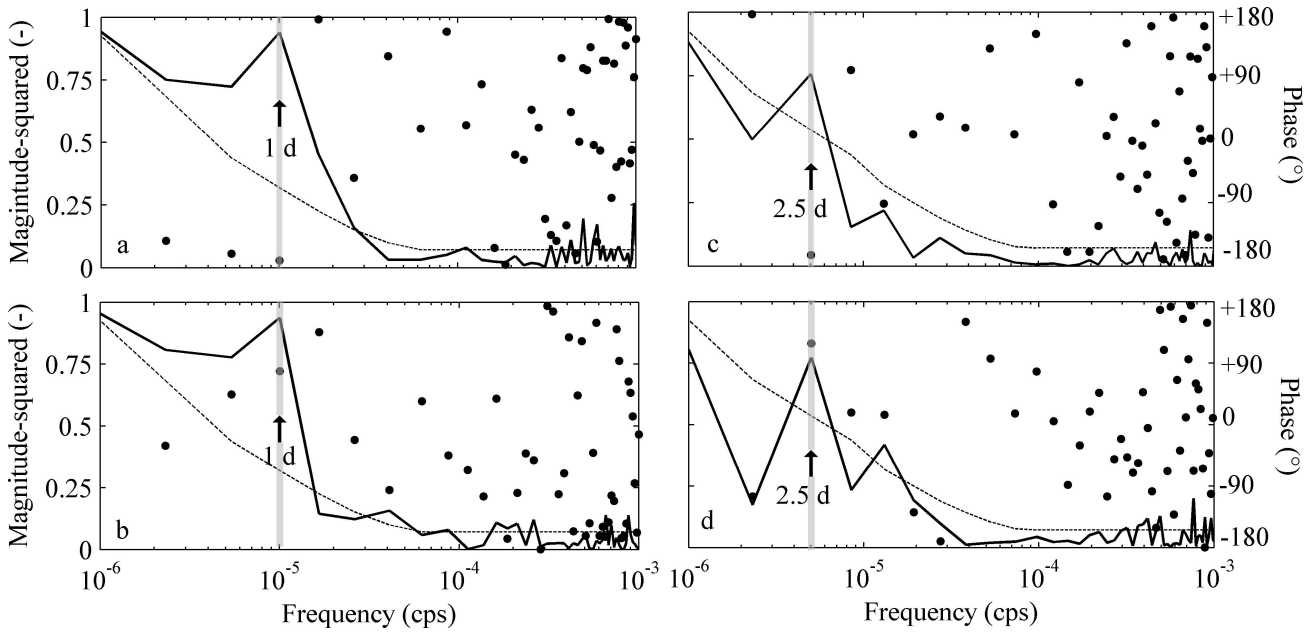

Fig. 9. Coherence and phase spectra of (a) the 20°C isotherm oscillations recorded at LDS and TC1 locations, (b) the 20°C isotherm oscillations and the SN component of the wind recorded at LDS, (c) the metalimnion thickness at LDS and TC1, and (d) the metalimnion thickness and the SN component of the wind recorded at LDS. Dashed line shows the 95% confidence level; frequencies are expressed on the x axis in cycles per second (cps); gray-shaded areas highlight some frequencies of particular relevance, expressed in days (d).

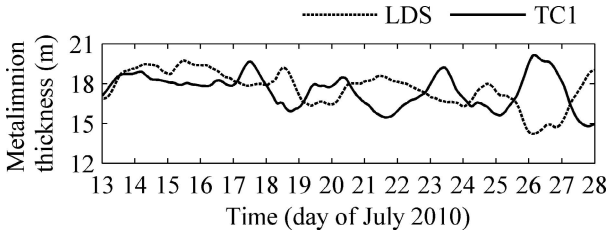

Fig. 10. Record of the metalimnion thickness (assumed to be the vertical distance between the 8°C and 18°C isotherms) measured at LDS and TC1 locations and low-passed with a cutoff period of 2 d.

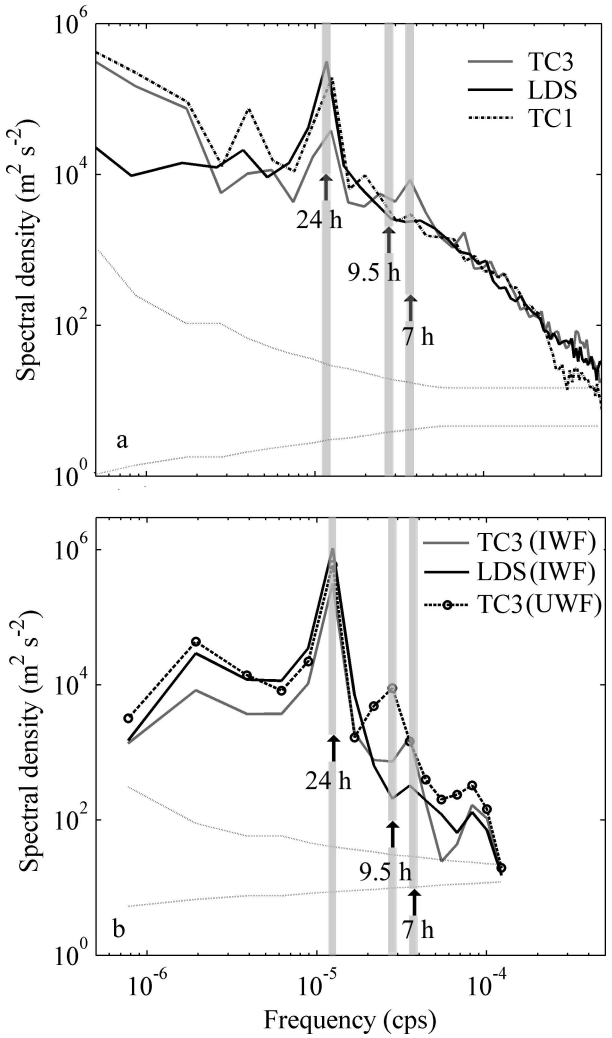

Fig. 11. Spectra of (a) the temperature signal measured at 10-m depth at LDS, TC1, and TC3 locations in the period 31 July–02 September 2010, and spectra of (b) the thermocline oscillations simulated at the LDS and TC3 locations by imposing the IWF and UWF in the period 01–15 August 2010. The 95% confidence level is shown by the two thin lower lines; frequencies are expressed on the x axis in cycles per second (cps); gray-shaded areas highlight some frequencies of particular relevance, expressed in hours (h). Both axes have a logarithmic scale.

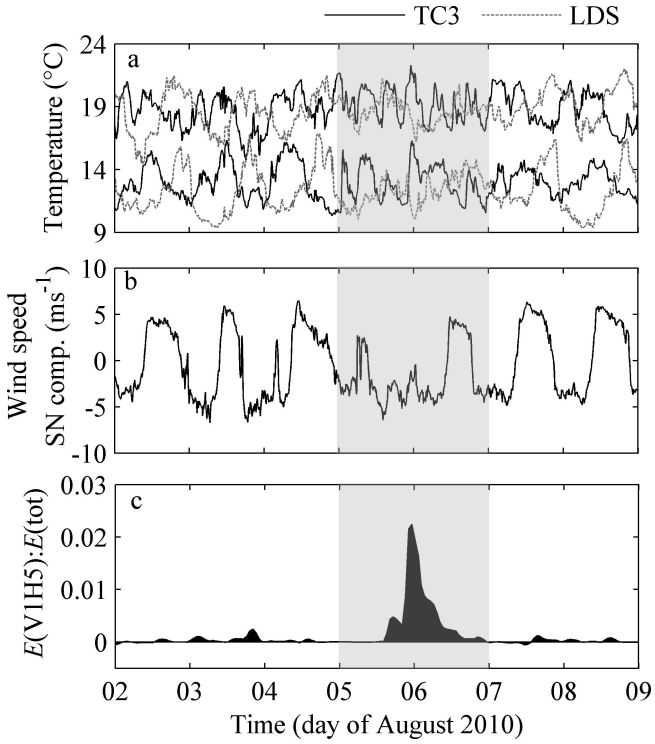

Fig. 12. (a) Temperature fluctuations measured at the TC3 and LDS locations at 10-m and 15-m depths, (b) SN component of the wind measured at the LDS location, and (c) simulated relative energetic contribution E of V1H5 mode with respect to the whole (tot) energy. Gray-shaded areas mark a distinctive occurrence of higher horizontal modes.

oscillation of the two metalimnion interfaces with a 56.4-h period. Both interface deflections demonstrated a uninodal horizontal structure with two antinodes at the lake extremes; the deeper fluctuations were characterized by larger amplitudes and a 180° phase shift with respect to the upper ones. The excitation of this mode induced a vertical squeezing and stretching of the intermediate layer in accordance with the field data: it closed and opened at the TC1 location on 25 and 26 July, respectively, while behaving anti-synchronously at the LDS location (*see* Fig. 10).

The same result was obtained by imposing a UWF (*see* Fig. 14c), suggesting that there were not relevant connections between this phenomenon and the spatial distribution of the forcing. On the contrary, the strong coherence between the observed metalimnion thickness recorded at LDS and the SN component of the wind at the 2.5-d period (*see* Fig. 9d) indicated that the onset on 24 July of a northerly wind event that lasted for > 24 h, could also be a possible reason for second vertical modes excitation, as it would have introduced a long time scale. Moreover, for the whole duration of this wind event the forcing worked positively on the V2H1 mode, whose natural period is equal to 56.4 h, while the energetic contribution to V1H1 decreased after 24 July 2010 (*see* Fig. 14a) due to the lack of inversion of wind stress, demonstrating that the interruption of the daily periodicity of the forcing favored the excitation of the second vertical mode.

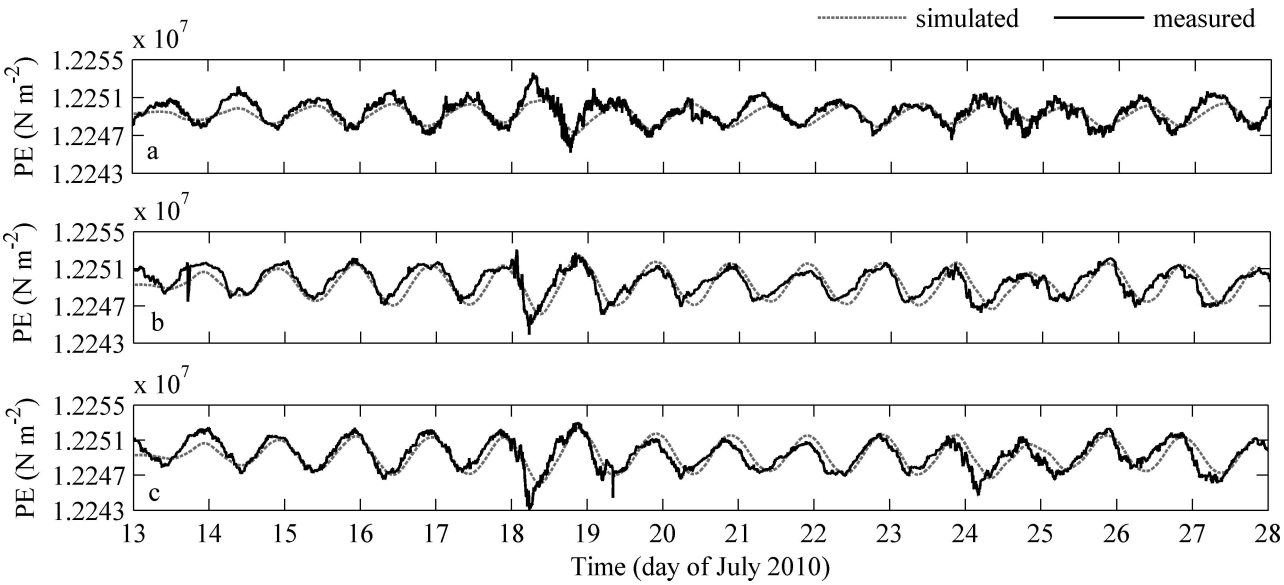

Fig. 13. Time series of the measured (continuous black lines) and simulated (gray dots) specific potential energy (PE) of the first 50 m at locations (a) LDS, (b) TC1, and (c) TC2.

Regarding the higher horizontal modes, the model reproduced the occasional excitation of V1H5 and V1H2 modes, that reached up to a maximum share of 1% and 3%, respectively (*see* Fig. 14b). By contrast, as shown in Fig. 14c, under the action of the UWF, V1H3 was excited.

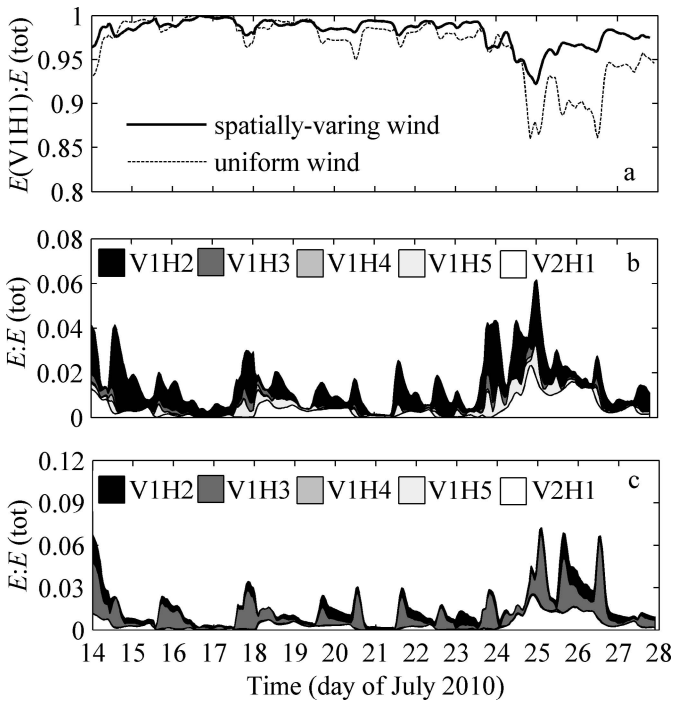

Fig. 14. Simulated partitioning of total (tot), potential plus kinetic, energy E between the different modes: (a) relative contribution of mode V1H1 under the action of a spatially varying (IWF) and uniform (UWF) wind field; relative contribution of modes V2H1, V1H2, V1H3, V1H4, and V1H5 with reference to the simulations carried on by imposing the (b) IWF and (c) UWF. (b–c) Note that the areas are cumulatively added.

In order to investigate V1H5 mode excitation, a simulation was carried out for the period 01–15 August 2010, with the IWF and the layered structure described in Table 2. The results are shown in Fig. 11b for the LDS and TC3 locations. Consistently with the field observations, both the dominant wave signals were observed at diurnal frequency, but at the station near Monte Isola a second energy peak might be clearly observed at around 7 h, corresponding to mode V1H5 (*see* Table 3). A further confirmation came from the temporal evolution of the modal energy; Fig. 12c shows that the contribution of V1H5 mode strongly increased on 05–06 August 2010, simultaneously with the observed amplification of the 7-h period wave motions around the island. Both the period and the spatial distribution of the wind field conditioned the occurrence of this wave motion. Figure 12b reveals that on 05–06 August 2010 the ordinary wind was interrupted by a northerly wind characterized by a sub-daily periodicity close to the V1H5 one. With regard to the spatial scale, it is relevant to observe that the local excitation of V1H5 diminished when the UWF measured at the LDS station was introduced in the model; under this condition, the secondary peak simulated at TC3 location shifted to the V1H3 natural period (around 9.5 h; *see* Fig. 11b), coherently with the splitting of the integral rate of work by different wind fields already observed in July (*see* Fig. 14b–c).

Theoretical analysis of V1H5 mode response—The role of Lake Iseo bathymetry on the internal wave structure was analyzed by comparing the wave motion with and without the presence of the island, the latter (not shown due to space constraints) obtained for a domain where a bottom fixed at 80 m took the place of Monte Isola. This showed that the presence of the island caused a break in symmetry between the five cells of mode H5, greatly magnifying the vertical displacements of the layer interface in the area

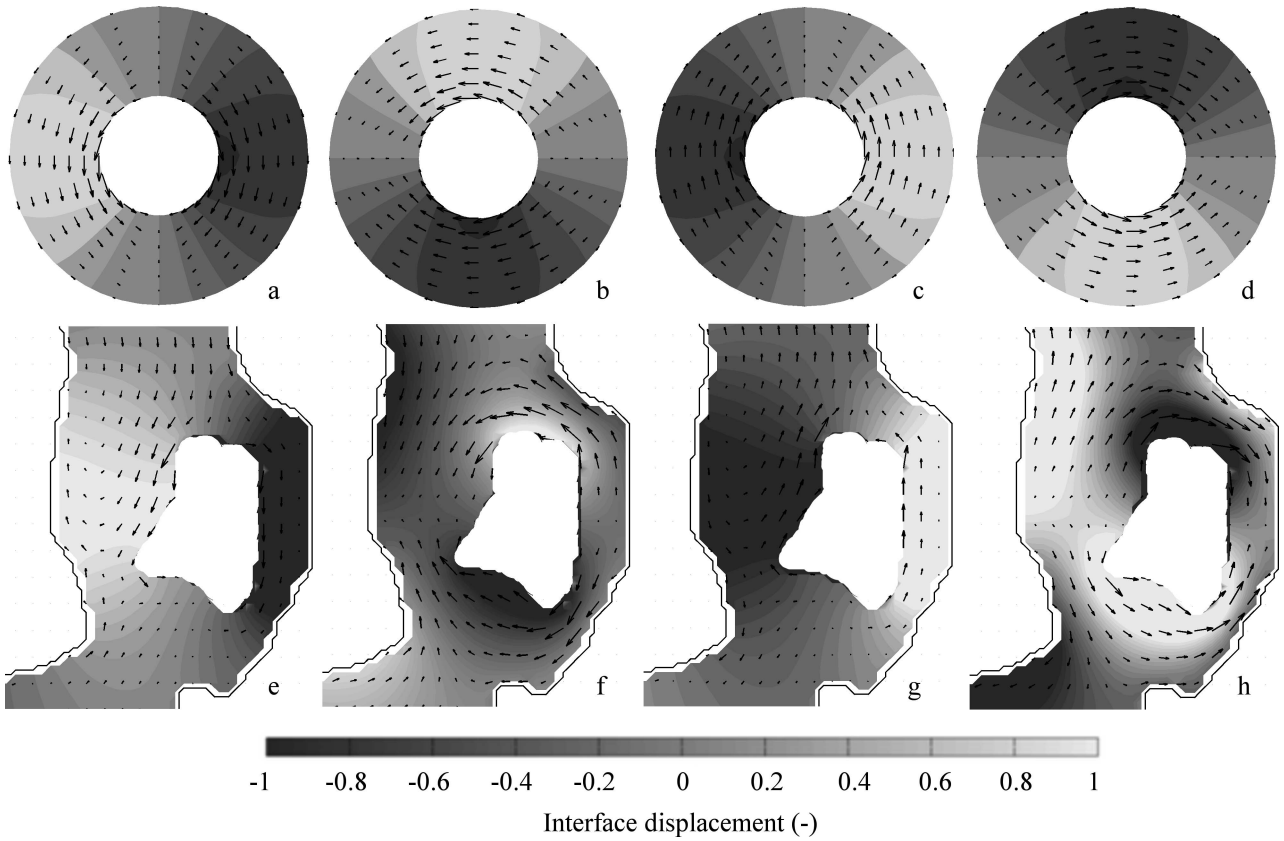

Fig. 15. Comparison between (a–d) the analytical solution obtained for the anticyclonic wave in flat annular basin lake with R_2 = 2500 m, R_1 = 1000 m, and S = 1.81, and (e–h) the V1H5 mode structure around Monte Isola. Each plot differs from the previous one by one-quarter of phase. The shading represents the nondimensional vertical displacements of the second layer upper interface displacement $\eta : \eta_{\max}$ with respect to the equilibrium level. The arrows show the average velocities of the upper layer.

around the island; mode H5 structure appeared as a peculiar mode of oscillation linked to the presence of Monte Isola. The motion due to this mode might be characterized as a clockwise-rotating wave with magnified velocities and wave amplitudes close to the island perimeter.

In light of this finding an interpretation of mode H5 might be proposed following the work by Stocker et al. (1987), which has been applied to multi-basin lakes as a dynamic explanation of the multicellular horizontal structure of free modes in circular or elliptic basins that fit the shape of a certain cell (Roget et al. 1997; Gomez-Giraldo et al. 2006; Shimizu et al. 2007). To interpret the clockwise wave rotating around Monte Isola, we investigated the basin-scale internal waves in an annular basin of constant depth. This theory widens the linear solution for superficial and internal seiches propagating in a rotating circular basin of constant depth given by Lamb (1932) and Csanady (1967) for a homogeneous and two-layer fluid, respectively, and extended to elliptical basins by Antenucci and Imberger (2001). Here we briefly describe the form of the deduced equations; the reader is referred to the Web Appendix (www.aslo.org/lo/toc/vol_57/issue_3/0772a.pdf) for details of the mathematical derivation. The dispersion wave equation that provides the super-inertial (“Poincaré mode”) angular frequency of the wave motion ω in a rotating annular basin takes the form:

$$N[J_{n-1}(N) - \Psi Y_{n-1}(N)] + n\left(\frac{1}{\sigma_j} - 1\right)[J_n(N) - \Psi Y_n(N)] = 0 \tag{7}$$

where j is the vertical mode number, n the azimuthal mode number, and $\sigma_j = \omega_j/f$ the nondimensional frequency. The terms N and Ψ, respectively, take into account the effects of the rotation and the shape of the annulus through the Burger number S_j and the geometrical ratio between the outer (R_2) and inner (R_1) radius $\chi = R_2/R_1$ (*see* Web Appendix, Eqs. A10 and A11 for their expression). When the Bessel functions of first and second type J and Y are exchanged with the corresponding modified Bessel functions I and K, Eq. 7 provides the sub-inertial (“Kelvin mode”) frequencies. Once the roots of Eq. 7 have been found, the modal pressure π_j, assumed periodic in time t and azimuthal coordinate θ, can be obtained, solving:

$$\pi_j = G_j(r)\cos(n\theta)\cos(\omega_j t) \tag{8}$$

while the modal transport fields are given by Csanady (1967):

$$\begin{cases} U_j^r = \dfrac{-gD_j}{\omega_j^2 - f^2}\left(\omega_j \dfrac{\partial G_j(r)}{\partial r} + \dfrac{fn}{r} G_j(r)\right)\sin\left(n\theta + \omega_j t\right) \\ U_j^\theta = \dfrac{-gD_j}{\omega_j^2 - f^2}\left(\omega_j \dfrac{\partial G_j(r)}{\partial r} + \dfrac{\omega_j n}{r} G_j(r)\right)\cos\left(n\theta + \omega_j t\right) \end{cases} \quad (9)$$

where r is the radial coordinate, D_j is an equivalent depth, representing the depth of a homogeneous fluid barotropic long wave phase whose speed matches the baroclinic speed of the internal wave vertical mode under consideration, $G_j(r)$ and $\partial G_j(r)/\partial r$ are the modal pressure in an annulus and its radial derivative (*see* Web Appendix, Eqs. A2 and A7 for details).

In Fig. 15 the cell that forms in the area around Monte Isola was compared with the first azimuthal-free mode that forms in an annulus with outer and inner radii of 2500 and 1000 m, respectively, a flat bottom 200 m deep, and a Burger number equal to 1.8. In both the domains it is possible to observe a wave rotating clockwise with maximum potential and kinetic energy close to the island. Figure 15 shows that the main features of both the amplitude and the velocity structure around Monte Isola were well reproduced by the analytical solution of the anticyclonic wave. Good agreement was observed also in terms of wave periods, even though the analytical solution slightly overestimates the frequency of the V1H5 mode (6.7 h).

The schematic annulus case demonstrated that the H5 mode in Lake Iseo was a Poincaré-like wave, anchored by Monte Isola as a consequence of the fit between the wavelength and a geometrical length-scale that characterizes the annulus. The role of the domain shape and the resulting wave spectrum is well known in other fields of dynamics, and a good analogy is the design of violins, where not only the choice of timber and its wall thickness are known to be important, but also the shape of the case (Moral and Jansson 1980).

Discussion

The main result from this investigation is that internal wave modes are excited whenever the spatial and temporal structure of a wind field over a lake matches the surface velocity field of a particular internal mode. In Lake Iseo, this match was predominantly with the 24.5-h fundamental mode V1H1; occasionally higher vertical modes (V2H1) and locally higher horizontal modes (V1H5) were excited, but their energies were generally $< 5\%$ of that of the total response. The duration of the wind forcing was shown to be the main factor controlling the excitation of second vertical modes. These results extend the results presented by Münnich et al. (1992), Antenucci and Imberger (2003), and Vidal et al. (2007), who reported resonance when the forcing frequency matched the oscillation frequency.

The spatial distribution of the wind field in the lake acts as a separator for modes that have similar natural periods and thus controls the excitation of higher horizontal modes, as already observed in other case studies (Wang et al. 2000; Lemmin et al. 2005; Okely et al. 2010). During the experimental period, the model with the IWF as a boundary condition showed a relevant energetic contribution of the second and fifth horizontal mode, due to the spatial fit between wind and modal wave structure. This setting, in particular, guaranteed the reproduction of the V1H5 signal captured by the T-chain measurements nearby Monte Isola, whose simulation was possible only taking into account the effects of the island on the wind field. This result has two main implications. First, it provides justification of the choice of the internal wave modeling in the lake by means of a spatially varying distribution of the surface stress and, second, it illustrates the important effect of the lake morphology on the basin-scale internal wave structure. The Poincaré-like wave trapped by Monte Isola appears as an oscillatory motion connected by the peculiar Lake Iseo morphometry, detachable locally nearby the island and excitable by the spatially varying wind field that characterizes this site as a consequence of the topography that surrounds the basin. This might be relevant to the benthic boundary layer flux, as it is energized by the local, above-bed velocity field as previously documented in Lake Kinneret by Marti and Imberger (2006).

Acknowledgments

We acknowledge the overall support of the Consorzio di Gestione Associata dei Laghi d'Iseo, Endine e Moro that made this research possible. We also acknowledge the financial support of the Australian Research Council Discovery Project DP1096728 and of the Fondazione della Comunità Bresciana Onlus. We finally thank the reviewers and the editor, whose suggestions contributed to improve the quality of this paper. This article represents the Centre for Water Research reference 2357-GV.

References

Antenucci, J. P., and J. Imberger. 2001. Energetics of long internal gravity waves in large lakes. Limnol. Oceanogr. **46:** 1760–1773, doi:10.4319/lo.2001.46.7.1760

———, and ———. 2003. The seasonal evolution of wind/internal wave resonance in Lake Kinneret. Limnol. Oceanogr. **48:** 2055–2061, doi:10.4319/lo.2003.48.5.2055

———, ———, and A. Saggio. 2000. Seasonal evolution of the basin-scale internal wave field in a large stratified lake. Limnol. Oceanogr. **45:** 1621–1638, doi:10.4319/lo.2000.45.7.1621

Bäuerle, E. 1985. Internal free oscillations in the Lake of Geneva. Ann. Geophys. **3:** 199–206.

———. 1994. Transverse baroclinic oscillations in Lake Überlingen. Aquat. Sci. **56:** 145–160, doi:10.1007/BF00877205

Becker, J., and J. Miles. 1991. Standing radial cross-waves. J. Fluid Mech. **222:** 471–499, doi:10.1017/S0022112091001180

Bini, A., D. Corbari, P. Falletti, M. Fassina, C. Perotti, and A. Piccin. 2007. Morphology and geological setting of Iseo lake (Lombardy) through multibeam bathymetry and high-resolution seismic profiles. Swiss J. Geosci. **100:** 23–40, doi:10.1007/s00015-007-1204-6

Chubarenko, B. V., Y. Wang, L. P. Chubarenko, and K. Hutter. 2001. Wind-driven current simulations around the Island Mainau (Lake Constance). Ecol. Model. **138:** 55–73, doi:10.1016/S0304-3800(00)00393-8

Csanady, G. T. 1967. Large-scale motions in Great Lakes. J Geophys. Res. **7:** 4151–4162, doi:10.1029/JZ072i016p04151

Defant, F. 1951. Local winds, p. 663–665. *In* T. M. Malone [ed.], Compendium of meteorology. American Meteorological Society.

de Franceschi, M., G. Rampanelli, and D. Zardi. 2002. Further investigations of the Ora del Garda valley wind, p. 30–33. *In* 10th Conference on Mountain Meteorology and Mesoscale Alpine Programme MAP-Meeting, June 2002, Park City, Utah. American Meteorological Society. Online at ams.confex.com/ams/pdfpapers/39949.pdf

de la Fuente, A., K. Shimizu, J. Imberger, and Y. Nino. 2008. The evolution of internal waves in a rotating, stratified, circular basin and the influence of weakly nonlinear and nonhydrostatic accelerations. Limnol. Oceanogr. **53:** 2738–2748, doi:10.4319/lo.2008.53.6.2738

Fappani, A. 2005. Venti. Enc. Bresciana **20:** 353–345.

Forcat, F., E. Roget, M. Figueroa, and X. Sánchez. 2011. Earth rotation effects on the internal wave field in a stratified small lake: Numerical simulations. Limnetica **30:** 27–42.

Fricker, P., and H. Nepf. 2000. Bathymetry, stratification, and internal seiche structure. J. Geophys. Res. **105:** 14237–14251, doi:10.1029/2000JC900060

Gomez-Giraldo, A., J. Imberger, and J. P. Antenucci. 2006. Spatial structure of the dominant basin-scale internal waves in Lake Kinneret. Limnol. Oceanogr. **51:** 229–246, doi:10.4319/lo.2006.51.1.0229

Hodges, B. R., J. Imbeger, A. Saggio, and K. B. Winters. 2000. Modeling basin-scale internal waves in a stratified lake. Limnol. Oceanogr. **45:** 1603–1620, doi:10.4319/lo.2000.45.7.1603

Horn, D., J. Imberger, and G. N. Ivey. 2001. The degradation of long-scale interfacial gravity waves in lakes. J. Fluid Mech. **434:** 181–207, doi:10.1017/S0022112001003536

Horn, W., C. H. Mortimer, and D. J. Schwab. 1986. Wind-induced internal seiches in Lake Zürich observed and modelled. Limnol. Oceanogr. **31:** 1232–1254, doi:10.4319/lo.1986.31.6.1232

Imberger, J. 1998. Flux paths in a stratified lake: A review, p. 1–18. *In* J. Imberger [ed.], Physical processes in lakes and oceans. American Geophysical Union.

———. 2004. A lake diagnostic system for managing lakes and reservoirs. Water Resour. Impact **6:** 7–10.

Kodomari, S. 1984. Studies on the internal wave in small lakes. II. Effect of lake basin shape in the internal wave. Jpn. J. Limnol. **45:** 269–278, doi:10.3739/rikusui.45.269

Lamb, H. 1932. Hydrodynamics. 6th ed. Dover.

Laval, B., J. Imberger, B. R. Hodges, and R. Stocker. 2003. Modelling circulation in lakes: Spatial and temporal variations. Limnol. Oceanogr. **48:** 983–994, doi:10.4319/lo.2003.48.3.0983

Lemmin, U., and N. D'Adamo. 1996. Summertime winds and direct cyclonic circulation: Observations from Lake Geneva. Ann. Geophys. **14:** 1207–1220.

———, C. H. Mortimer, and E. Bäuerle. 2005. Internal seiche dynamics in Lake Geneva. Limnol. Oceanogr. **50:** 207–216, doi:10.4319/lo.2005.50.1.0207

Marti, C. L., and J. Imberger. 2006. Dynamics of the benthic boundary layer in a strongly forced stratified lake. Hydrobiologia **568:** 217–233, doi:10.1007/s10750-006-0111-6

———, and ———. 2008. Exchange between littoral and pelagic waters in a stratified lake due to wind induced motions: Lake Kinneret, Israel. Hydrobiologia **603:** 25–51, doi:10.1007/s10750-007-9243-6

Moral, J. A., and E. V. Jansson. 1980. Eigenmodes and the function of the violin. J. Catgut Acoust. Soc. **34:** 29–32.

Mortimer, C. H. 1952. Water movements in lakes during summer stratification: Evidence from the distribution of temperature in Windemere. Phil. Trans. R. Soc. Lond. A Math. Phys. Sci. **236:** 355–404, doi:10.1098/rstb.1952.0005

———. 1953. The resonant response of stratified lakes to wind. Schweiz. Z. Hydrol. **15:** 94–151, doi:10.1007/BF02486219

———. 1974. Lakes hydrodynamics. Mitt. Int. Verein. Limnol. **29:** 124–197.

Münnich, M., A. Wueest, and D. M. Imboden. 1992. Observations of the second vertical mode of the internal seiche in an alpine lake. Limnol. Oceanogr. **37:** 1705–1719, doi:10.4319/lo.1992.37.8.1705

Okely, P. N., J. Imberger, and K. Shimizu. 2010. Horizontal dispersion due to interplay of motions in the surface layer of a small reservoir. Limnol. Oceanogr. **55:** 589–603, doi:10.4319/lo.2009.55.2.0589

Platzman, G. 1972. Two-dimensional free oscillations in natural basins. J. Phys. Oceanogr. **2:** 117–138, doi:10.1175/1520-0485(1972)002<0117:TDFOIN>2.0.CO;2

Roget, E., G. Salvadè, and F. Zamboni. 1997. Internal seiche climatology in a small lake where transversal and second vertical modes are usually observed. Limnol. Oceanogr. **42:** 663–673, doi:10.4319/lo.1997.42.4.0663

Rueda, F. J., S. G. Schladow, S. Monismith, and M. Stacey. 2005. On the effects of topography on wind and the generation of currents in a large multi-basin lake. Hydrobiologia **532:** 139–151, doi:10.1007/s10750-004-9522-4

———, ———, and S. O. Palmarsson. 2003. Basin-scale internal wave dynamics during a winter cooling period in a large lake. J. Geophys. Res.-Oceans **108:** 3097, doi:10.1029/2001JC000942

Schwab, D. J. 1977. Internal free oscillation in Lake Ontario. Limnol. Oceanogr. **22:** 700–708, doi:10.4319/lo.1977.22.4.0700

Shimizu, K., and J. Imberger. 2008. Energetics and damping of basin-scale internal waves in a strongly stratified lake. Limnol. Oceanogr. **53:** 1574–1588, doi:10.4319/lo.2008.53.4.1574

———, ———, and M. Kumagai. 2007. Horizontal structure and excitation of primary motions in a strongly stratified lake. Limnol. Oceanogr. **52:** 2641–2655, doi:10.4319/lo.2007.52.6.2641

Stocker, K., K. Hutter, G. Salvadé, J. Trösch, and F. Zamboni. 1987. Observations and analysis of internal seiches in the southern basin of Lake Lugano. Ann. Geophys. **6:** 553–568.

Strub, P. T., and T. M. Powell. 1986. Wind-driven surface transport in stratified closed basins: Direct versus residual circulation. J. Geophys. Res. **91:** 8497–8508, doi:10.1029/JC091iC07p08497

Vidal, J., F. Rueda, and X. Casamitjana. 2007. The seasonal evolution of high vertical-mode internal waves in a deep reservoir. Limnol. Oceanogr. **52:** 2656–2667, doi:10.4319/lo.2007.52.6.2656

Wang, Y., K. Hutter, and E. Bäuerle. 2000. Wind-induced baroclinic response of Lake Constance. Ann. Geophys. **18:** 1488–1501, doi:10.1007/s00585-000-1488-6

Associate editor: Craig L. Stevens

Received: 14 June 2011
Accepted: 23 February 2012
Amended: 29 October 2011